processes

MDPI

Article

Comparison of Packed-Bed and Micro-Channel Reactors for Hydrogen Production via Thermochemical Cycles of Water Splitting in the Presence of Ceria-Based Catalysts

Nonchanok Ngoenthong [1], Matthew Hartley [2], Thana Sornchamni [3], Nuchanart Siri-nguan [3], Navadol Laosiripojana [4] and Unalome Wetwatana Hartley [1,4,*]

1 Chemical and Process Engineering, The Sirindhorn International Thai-German Graduate School of Engineering (TGGS), King Mongkut's University of Technology North Bangkok, Bangkok 10800, Thailand; nonchanok.n-cpe2015@tggs-bangkok.org
2 Chemical Engineering Department, Engineering Faculty, King Mongkut's University of Technology North Bangkok, Bangkok 10800, Thailand; matthew.m.hartley@gmail.com
3 PTT Public Company Limited, 555 Vibhavadi Rangsit Road, Chatuchak, Bangkok 10900, Thailand; thana.s@pttplc.com (T.S.); nuchanart.s@pttplc.com (N.S.-n.)
4 Joint Graduate School of Energy and Environment (JGSEE), King Mongkut's University of Technology Thonburi, Bangkok 10140, Thailand; navadol@jgsee.kmutt.ac.th
* Correspondence: unalome.w.cpe@tggs-bangkok.org

Received: 26 August 2019; Accepted: 15 October 2019; Published: 18 October 2019

Abstract: Hydrogen production via two-step thermochemical cycles over fluorite-structure ceria (CeO_2) and ceria-zirconia ($Ce_{0.75}Zr_{0.25}O_2$) materials was studied in packed-bed and micro-channel reactors for comparison purposes. The H_2-temperature program reduction (H_2-TPR) results indicated that the addition of Zr^{4+} enhanced the material's reducibility from 585 μmol/g to 1700 μmol/g, although the reduction temperature increased from 545 to 680 °C. $Ce_{0.75}Zr_{0.25}O_2$ was found to offer higher hydrogen productivity than CeO_2 regardless of the type of reactor. The micro-channel reactor showed better performance than the packed-bed reactor for this reaction.

Keywords: hydrogen production; thermochemical cycles; micro-channel reactor; ceria; ceria-zirconia; water splitting; oxygen carrier

1. Introduction

Hydrogen can be utilized in many modern-world applications. Its well-known challenges include production cost, transportation and storage. Hydrogen can be produced by various means, e.g., thermochemical processes, reforming processes, gasification, electrolysis, biological processes, and so on [1–8]. Conventional hydrogen production from either natural gas, coal, or biomass appears to be the most commercially available and affordable, although this unavoidably releases carbon emissions, radioactive elements, and air-borne pollutions into the atmosphere. Hydrogen production from water is a green technology in which water is split, producing high-purity gaseous hydrogen. Recent water splitting processes including, for instance, photo-catalytic, two-step thermochemical cycles, electrolysis and biological processes have been employed to generate high-purity hydrogen. The two-step thermochemical cycle possesses advantages over the others in terms of the product's purity and yield [9]. The two-step thermochemical cycle reaction consists of (1) endothermic reduction, where the metal oxide material is reduced by thermal energy and/or chemical reducing agents, resulting in gaseous oxygen as a by-product and an active and non-stoichiometric reduced metal oxide, (2) exothermic oxidation, where the active metal oxides are oxidized by water, giving high-purity hydrogen

as a product while the metal oxide is recycled back into its original stage [10–12]. The operating conditions—i.e., temperature, feed reactant and reaction time—of the two steps are different. Thus, the process can either be carried out in (1) two reactors between which the solid material is moved, or (2) one reactor in which the operating conditions are switched back and forth from the reduction to the oxidation step. The former is suitable for solid materials that have high mechanical strength, have changed phase, and have been fully reduced/oxidized based on their stoichiometry, such as ZnO/Zn [13], CdO/Cd [14], SnO_2/SnO [15], and GeO_2/GeO [16], although the process requires a sophisticated quenching and control system. The latter is commonly used with materials with no phase change. The materials could be either stoichiometric redox materials such as Fe_3O_4/FeO [17], MFe_2O_4 [18], and $CoFe_2O_4/Al_2O_3$ [19], or non-stoichiometric redox materials such as, for example, ceria and ceria-based materials [20–22], and perovskites [23]. Ceria (CeO_2) and ceria-zirconia (CeO_2/ZrO_2) were selected as the oxygen carrier in this work, as they offer (1) high oxygen storage capacity [24,25], (2) high thermal stability, and (3) the possibility of being fabricated as the whole reactor itself. Although the latter process does not require a quenching system and complicated fluidized bed operation, it needs a well-established control system that allows the operational conditions to switch from reduction to oxidation steps precisely. Regardless of the quality of the control system, the switching between conditions (temperature, feed) still causes low overall process efficiency (10 to 50%) [26–29]. Therefore, a reactor that offers rapid heat and mass transfer during the change is beneficial for this process. Additionally, the redox materials must be able to withstand the severe condition swing. This work studied the process under the same reduction and oxidation temperature, aiming to (1) optimize the process efficiency and product yield, (2) ease the control system, and (3) make it possible to use wider variety of the new catalysts. A micro-channel reactor was also applied to enable rapid mas/heat transfer, with shorter residence time.

2. Methodology

2.1. Catalyst Preparation, Substrate Pretreatment and Catalyst Coating

2.1.1. Catalyst Preparation

Nitrate precursors of Ce and Zr were mixed with 0.1 M cetyl trimethyl ammonium bromide (CTAB) at room temperature while NaOH was added dropwise, keeping pH at 11 while stirring. Molar ratio of CTAB to total cations (Ce + Zr) was fixed at 0.8. The mixture was centrifuged at 4000 rpm for 10 min, and then washed with de-ionized water to remove any possible impurities. The precipitate was dried in the oven at 120 °C overnight and calcined at 700 °C for 3 h in air with 2 °C/min heating rate. For the micro-channel reactor, alumina solution was additionally synthesized by hydrolysis of aluminum tri-sec-butoxide (Aldrich, St. Louis, MO, USA, 97%) with a molar ratio of H_2O to Al = 100 to enhance the adhesion force between the catalyst power and the surface of the substrate. The solution was peptized by adding nitric acid (HNO_3/Al = 0.07) and refluxed at 85 °C for 20 h. After that, nitrate precursors of Ce and Zr were dissolved into the prepared alumina solution. The mixed solution was heated at 85 °C until a thixotropic solution was obtained. The gel was dried at 110 °C overnight and calcined at 800 °C for 6 h at a heating rate of 2 °C/min.

2.1.2. Stainless Steel Substrate Preparation

The lab-designed micro-structured stainless steel (316L) plates were commercially made (TGI, Chonburi, Thailand), as shown in Figure 1. Each substrate has 14 channels with 300 µm depth, 370 µm width and 25 mm length per channel. The plates were cleaned by etching with 20% citric acid in an ultrasonic bath for 30 min. They were subsequently annealed at 800 °C for 2 h in air to form a layer of mixed metal oxides for better adhesion strength.

2.1.3. Catalyst Coating

Polyvinyl alcohol was dissolved in deionized water while stirring at 400 rpm at 65 °C for 2 h. The solution was left overnight without stirring. The catalyst powder and acetic acid were added to the solution. The weight ratio of catalyst powder to water to binder to acid was 10 to 84 to 5 to 1. The resulting suspension was stirred at 65 °C for 2 h, cooled to room temperature, and subsequently stirred for 3 days. The non-coating area of the micro-structured stainless steel plates, such as the inlet and the outlet, were covered with the polymer film. The prepared suspension was wash-coated on the micro-channel substrate, then left to dry at room temperature for 6 h. After the removal of the polymer film, the substrate was dried in an oven at 120 °C and calcined at 500 °C for 3 h at a heating rate of 1 °C/min. The 2 micro-channel substrates were then laser-welded together. The gas inlet and outlet at the top and bottom were connected to 1/8-inch stainless steel tubing.

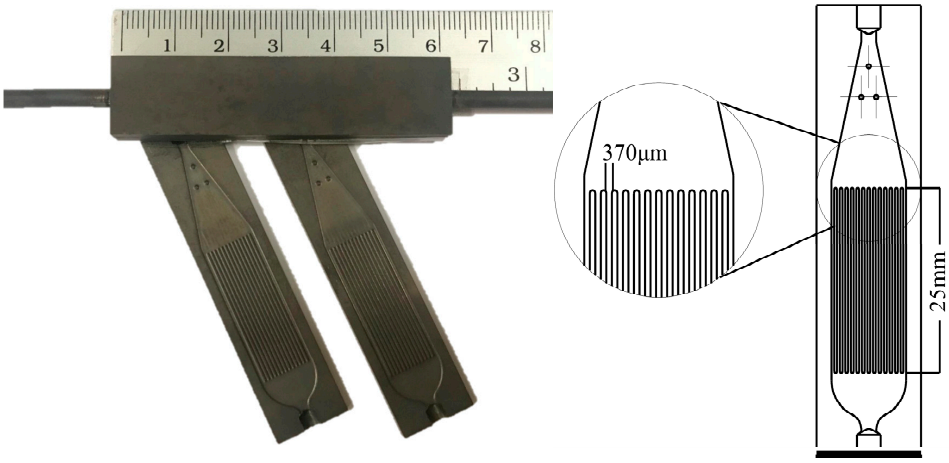

Figure 1. Stainless steel 316L micro-channeled plate.

2.2. Characterization

The crystallinity of the synthesized catalysts was characterized using X-ray diffraction (XRD). The morphology of the stainless steel substrates, before and after the annealing process at different temperatures, was characterized using scanning electron microscopy (SEM). The reduction temperature of the samples was investigated using the H_2-temperature program reduction technique (H_2-TPR). During the H_2-TPR, 10% H_2/Ar was passed through the catalyst's bed in the reactor. The temperature was increased from room temperature to 950 °C, at a heating rate of 5 °C/min, and held for 30 min. The gaseous products were analyzed using on-line mass spectrometer (MS, GSD 320 O1, OmniStar gas analysis) for all experiments.

2.3. Experimental Set-Up

The catalysts were pelletized and sieved to 180–212 μm for the packed-bed reactor, and <38 μm for the micro-channel reactor. The weight of the catalyst was 1 g and 8–15 mg for the packed-bed reactor and the micro-channel reactor, respectively. Each catalyst was placed inside the quartz tube packed-bed reactor (i.d. = 10 mm, length = 50 cm) between two layers of quartz wool. The packed-bed and micro-channel reactors were placed in the middle of an electrical furnace (Inconel, 20 cm heating zone). The schematic diagram of the experiments is shown in Figure 2. The system was purged by 300 mL/min of Ar using a mass flow controller (New Flow-TLFC-00-A-1-W-2, 10–500 mL/min) at room temperature for 1 h. Each catalyst was reduced before use in 10% H_2/Ar at 700 and 900 °C, in accordance with the TPR results, for 30 min. Steam was generated using a steam generator, whereby the amount of water was controlled by peristaltic pump (BT100M Model, 0.00067–65 mL/min). Steam was delivered to the reactor system through a 170 °C trace-heated line to prevent condensation. The total flow rate of 200 mL/min, which ensured the reaction control regime, was fixed for all of the experiments.

The reaction was isothermally operated at 700 and 900 °C. The gaseous product stream was analyzed using an on-line mass spectrometer (Quadrupole, Omnistar, GSD 320 O1 Model).

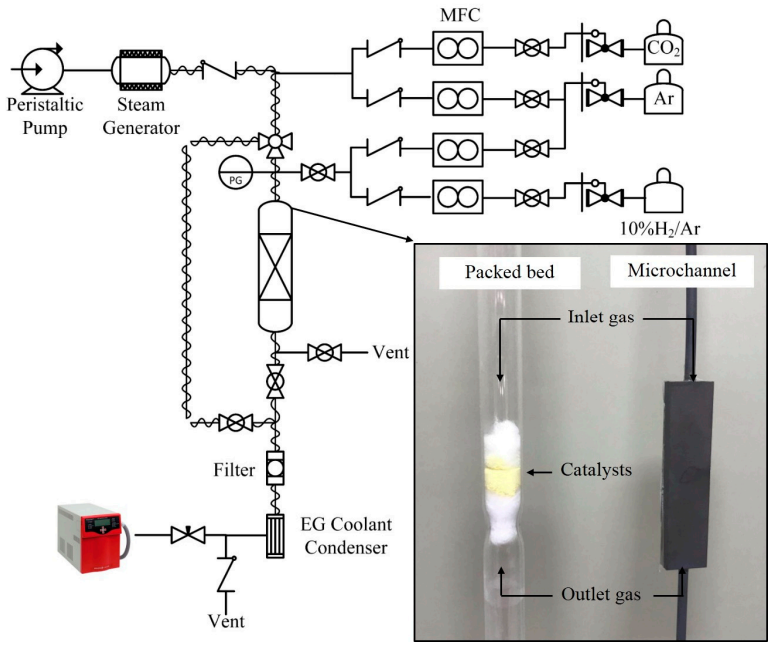

Figure 2. Rig schematic diagram for packed-bed and micro-channel process.

3. Result and Discussion

3.1. Characterization

Figure 3 shows diffractograms of all of the prepared catalysts, compared with pure alumina, shown as (a) CeO_2, (b) $Ce_{0.75}Zr_{0.25}O_2$, (c) 10%CeO_2/Al_2O_3, (d) 10%$Ce_{0.75}Zr_{0.25}O_2/Al_2O_3$, and (e) pure alumina.

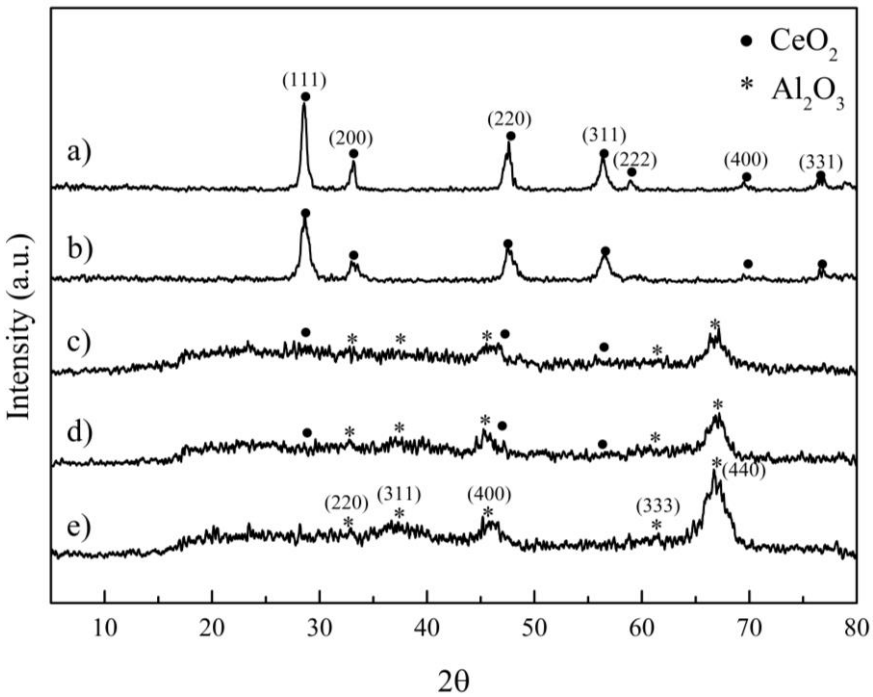

Figure 3. XRD patterns of (**a**) CeO_2, (**b**) $Ce_{0.75}Zr_{0.25}O_2$, (**c**) 10% CeO_2/Al_2O_3, (**d**) 10% $Ce_{0.75}Zr_{0.25}O_2/Al_2O_3$, and (**e**) pure alumina.

CeO_2 and $Ce_{0.75}Zr_{0.25}O_2$ possessed a fluorite cubic structure with a face-centered cubic crystal system (FCC), which offers a high thermal stability and oxygen exchange kinetic rate [30–32]. CeO_2 and $Ce_{0.75}Zr_{0.25}O_2$ presented a lattice plane corresponding to the (111), (200), (220), (311), (222), (400) and (331) [33,34]. Their average crystal size, calculated using the Scherer equation, was 15.15 nm and 9.01 nm, respectively. Pure alumina was η-alumina and had a bayerite structure. Each peak corresponded to the (220), (311), (400), (333), and (440) lattice planes [35,36]. Both 10% CeO_2/Al_2O_3 and 10% $Ce_{0.75}Zr_{0.25}O_2/Al_2O_3$ showed η-alumina bayerite structures as a major crystalline phase, while CeO_2 and $Ce_{0.75}Zr_{0.25}O_2$ showed them as minor crystalline phase. The non-alumina catalysts were selected for the further study.

CeO_2 and $Ce_{0.75}Zr_{0.25}O_2$ showed two main reduction peaks at different temperatures, shown in Figure 4. Ceria and ceria-zirconia started to be reduced at the same temperatures, with the first peak at 300 °C (peaks α) and the second peak at 650 °C (peaks β). However, broader reduction peaks were observed in the ceria-zirconia due to the larger amount of oxygen release in ceria-zirconia. This led to a higher average reduction temperature for ceria-zirconia (680 and 950 °C), when compared to ceria (545 and 900°C), respectively. The results agreed with previous works reported by other researchers [37–40]. The first peaks of both catalysts were defined as surface reduction, evidenced by the steep reduction peaks, while the second peaks comprised bulk reductions, which were much broader compared to the first peaks due to the much slower solid-state oxygen diffusion within the materials. From the H_2-TPR profiles of both catalysts, it can be seen that ceria-zirconia had a higher reduction rate than ceria, and released a higher amount of oxygen within the studied temperature range. The addition of Zr into the ceria catalyst system has been suggested to affect the material's cell volume, resulting in an increase in surface area [41–44]. The degree of the reduction, represented by the non-stoichiometric oxygen release (δ), is calculated and tabulated in Table 1. For CeO_2, the surface oxygen was released at 545 °C, giving δ at 0.046 (theoretically maximum at 0.5) and percentage of reduction at 9.34%, where the material was reduced to $CeO_{1.95}$. The second peak of CeO_2 showed that the bulk oxygen was reduced at 900 °C, giving 0.074 of δ, which is equal to a reduction of 14.64%. At this stage, the $CeO_{1.88}$ became $CeO_{1.94}$. Similarly, ceria-zirconia was surface reduced and bulk reduced at 680 °C and 950 °C, respectively. The first reduction peak represented a δ of 0.277, with a reduction degree of 54.40%, while the second peak gave a δ of 0.222, with a reduction degree of 44.46%. The non-stoichiometric molecular formula of the ceria-zirconia after being reduced at 950 °C was $Ce_{0.75}Zr_{0.25}O_{1.51}$. $Ce_{0.75}Zr_{0.25}O_2$ conclusively showed better performance, compared to ceria, in terms of reduction rate and reducibility.

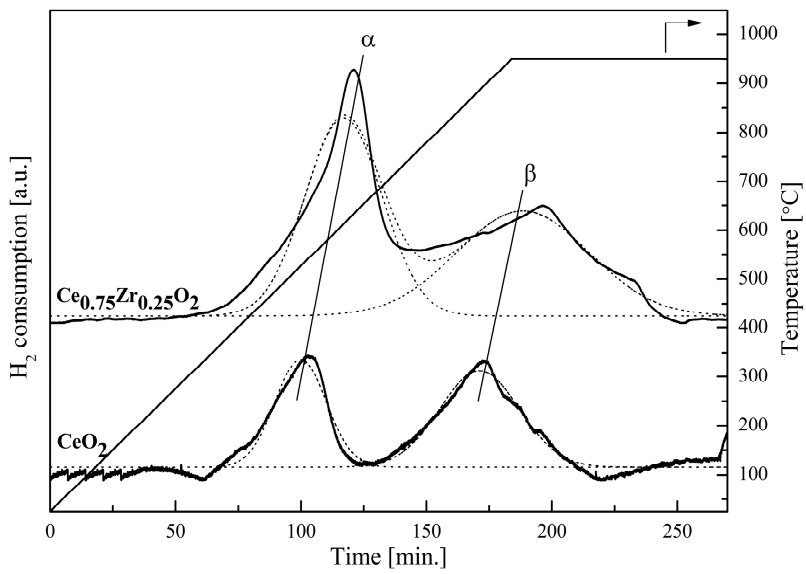

Figure 4. TPR profiles of CeO_2 and $Ce_{0.75}Zr_{0.25}O_2$ for temperatures ranging from 30 to 950 °C, at heating rate of 5 °C/min, using 10% H_2/Ar.

Table 1. H_2-TPR results of CeO_2 and $Ce_{0.75}Zr_{0.25}O_2$

Catalysts	Peak α			Peak β			Total OSC (μmol/g)	Total % Reduction (δ)
	T_{red} (°C)	OSC (μmol/g)	% Reduction (δ)	T_{red} (°C)	OSC (μmol/g)	% Reduction (δ)		
$CeO_{2-\delta}$	545	585	9.34% (δ = 0.046)	900	915	14.64% (δ = 0.074)	1500	23.98% (δ = 0.12)
$Ce_{0.75}Zr_{0.25}O_{2-\delta}$	680	1700	547.40% (δ = 0.272)	950	1390	44346% (δ = 0.222)	3090	98.86% (δ = 0.49)

Where OSC stands for oxygen storage capacity, calculated from H_2 consumption. The percentage of reduction degree is calculated using Equations (1)–(3) below:

$$\%X_{red} = \left(\frac{n_{[O]real}}{n_{[O]\max}}\right) \times 100 \quad (1)$$

$$n_{[O]real} = \frac{n_{H_2,consumed}}{m_{solid}} \quad (2)$$

$$n_{[O]\max} = \left(\frac{m_{solid}}{MW_{solid}}\right) \times \delta_{\max} \quad (3)$$

where $n_{[O]_{max}}$ is the maximum amount of O_2 release/uptake (mol/g) as a function of δ, δ is the stoichiometric coefficient of O in lattice (for this material, δ is 0.5 for maximum O release/uptake), $n_{[O]_{real}}$ is the number mole of O released per gram of the catalyst, which is equal to an integration of the area under the H_2 consumption curve, m_{solid} is the weight of the solid reactant, and MW_{solid} is the molecular weight of the catalyst [45].

Figure 5 shows the surface morphography of the prepared substrates (a) before and after annealing process at (b) 600, (c) 700, and (d) 800 °C. From the results, it can be seen that the oxides of the stainless steel's surface were formed by annealing, occurring best at the highest temperature: 800 °C.

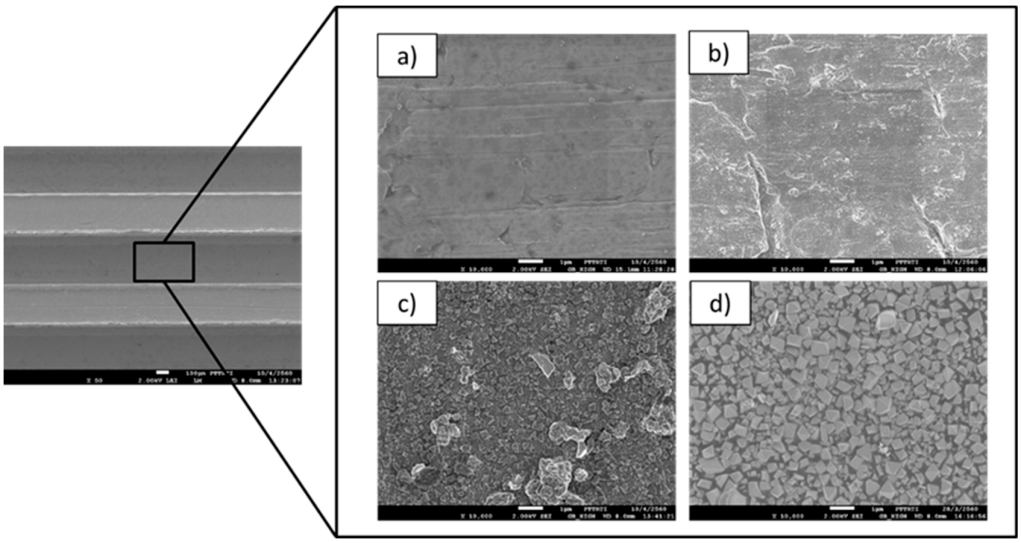

Figure 5. Morphology of the substrate surface analyzed using SEM technique: (**a**) before annealing and after annealing process at (**b**) 600, (**c**) 700, and (**d**) 800 °C.

Energy-dispersive X-ray spectroscopy technique (EDX) was applied to identify the oxides which were formed with metals consisting of the stainless steel. Table 2 presents the percentage of each element. The results suggested that the formation of oxides increased with an increase in annealing temperature, as evidenced by the higher percentage of oxygen. The results are in agreement with the SEM results, as reported in the previous section.

Table 2. Percentage of each element on the surface of the substrate.

Condition	O	Cr	Mn	Fe	Ni	Others	Total
Before annealing	7.69	28.61	–	47.87	5.65	10.18	100
Annealed at 600 °C	24.84	29.53	2.72	35.95	4.22	2.75	100
Annealed at 700 °C	30.04	26.34	–	30.44	3.75	9.43	100
Annealed at 800 °C	41.78	27.90	4.82	18.70	–	6.79	100

3.2. Catalytic Performance Experiments

3.2.1. Effect of ZrO_2 Addition

Catalytic performances of CeO_2 and $Ce_{0.75}Zr_{0.25}O_2$ towards the water splitting were tested in a packed bed reactor. The oxidation and reduction temperatures were paired at the same temperature to avoid temperature switching, aiming to maximize the overall process efficiency and minimize the thermal stress of the reactor. The selected temperatures of reduction and oxidation (Tred/Tox) were 700/700 and 900/900 °C.

From Figure 6, it can be seen that $Ce_{0.75}Zr_{0.25}O_2$ had better performance towards this reaction than CeO_2 for both selected temperatures. The effect was more obvious at the lower temperature (700 °C) than the higher temperature (900 °C). At 700 °C, the H_2 production of $Ce_{0.75}Zr_{0.25}O_2$ was 88.71% more than that produced via CeO_2 (increased from 483.42 to 912.26 μmol/g), although it was only 8.40% higher (increased from 1563.21 to 1694.55 μmol/g) at 900 °C. This result shared the same trend as previous work reported by Z. Zhao et al. [46], although both catalysts in this research offered around two times higher of H_2 productivity for both temperatures, which could be due to the benefit of a surfactant-assisted method which allows smaller fine particles and larger specific surface area [47].

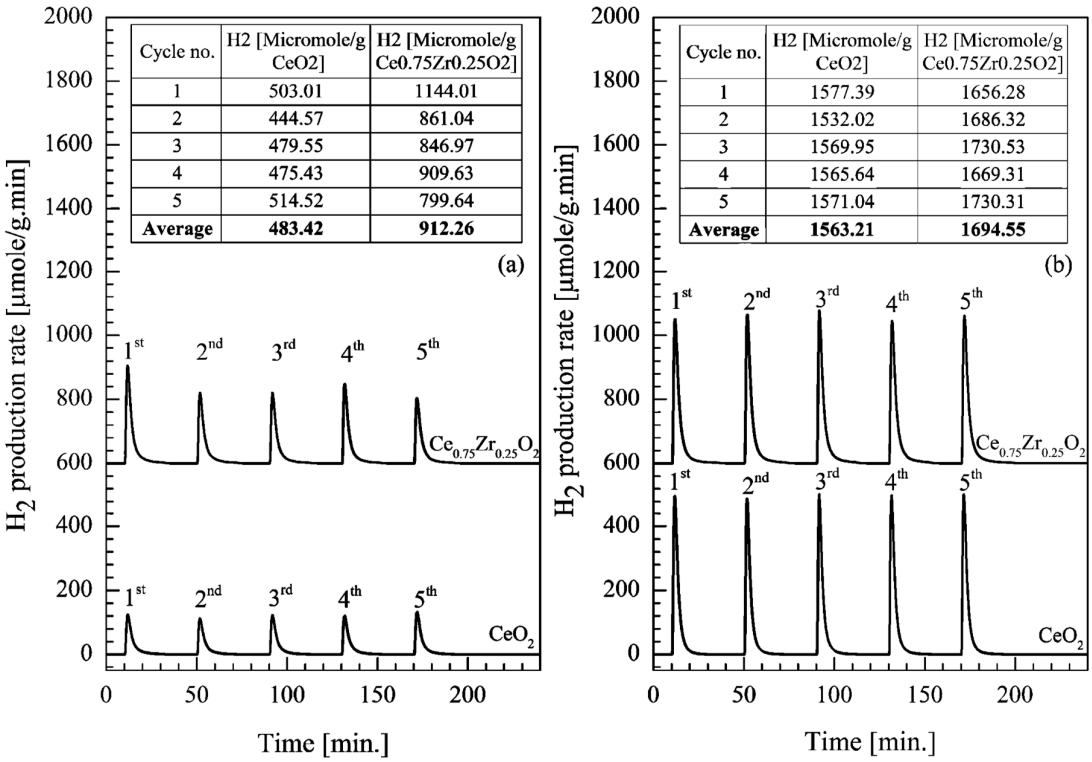

Figure 6. H_2 productivity over CeO_2 and $Ce_{0.75}Zr_{0.25}O_2$ in a packed-bed reactor, at the same reduction/oxidation temperature (**a**) 700/700 °C and (**b**) 900/900 °C.

3.2.2. Comparison of Micro-Channel Reactor and Packed-Bed Reactor

$Ce_{0.75}Zr_{0.25}O_2$ was selected for this experiment. H_2 production via both packed-bed and micro-channel reactors were compared. Uncoated micro-channel reactor was also introduced to the reactant stream and performed as a blank test. H_2 productivity in all experiments was calculated per weight of catalyst used. H_2 productivity from the blank micro-channel reactor, uncoated reactor, was subtracted from the catalyst-coated micro-channel reactor. The blank test was performed only for the micro-channel reactor, because the formation of metal oxides on the substrate surface after annealing, such as on Cr_2O_3, Mn_2O_3 and Fe_2O_3, could possibly be involved in the catalytic reaction. From Figure 7, the 5-cycle average amount of H_2 production using the packed-bed reactor and the micro-channel reactor was 912.26 and 14,308.32 µmol/g. Thus, micro-channel reactor showed roughly 16 times better performance than the packed-bed reactor, in terms of H_2 production. This was suggested to be the effect of its high surface-to-volume ratio, leading to an intrinsic reaction occurring at the molecular level [48–51]. It can be noticed that the H_2 productivity of the packed-bed reactor decreased while that of the micro-channel reactor increased when the number of cycles increased. The decrease in H_2 productivity in the packed-bed reactor was presumably due to the catalyst's coagulation when repetitively used at such temperatures. On the other hand, the increase in H_2 productivity in the micro-channel reactor was possibly the result of the reactive oxides, in which they were formed by the reaction of metals in the stainless steel and the oxygen in the system. Thus, the more cycles the reaction was run, the more H_2 productivity was achieved. However, these H_2 productivities in both type of reactor were supposed to be constant after a certain number of cycles.

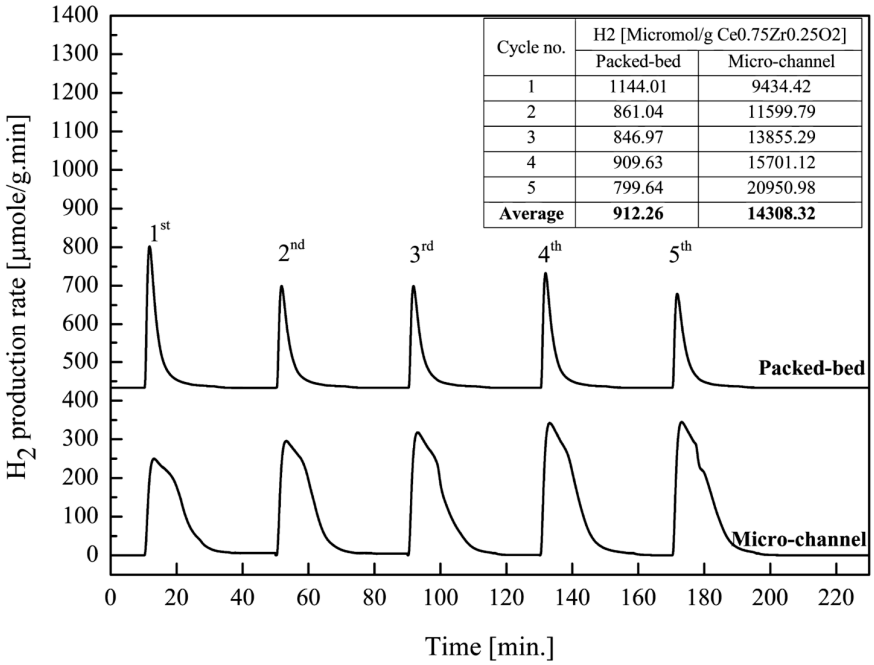

Cycle no.	H2 [Micromol/g Ce0.75Zr0.25O2]	
	Packed-bed	Micro-channel
1	1144.01	9434.42
2	861.04	11599.79
3	846.97	13855.29
4	909.63	15701.12
5	799.64	20950.98
Average	**912.26**	**14308.32**

Figure 7. Comparison of H_2 productivity over $Ce_{0.75}Zr_{0.25}O_2$ received from the micro-channel reactor and the packed-bed reactor at reduction/oxidation temperature at 700/700 °C.

In addition, the decline of the H_2 production rate in the micro-channel reactor was noticed to be much slower than that in the packed-bed reactor, leading to a longer reaction time. This was due to (1) the micro-channel reactor having a higher active surface area to volume, allowing better access of the reactants to the catalyst's surface, and (2) channeling and/or mass transfer limitation occurring in the packed-bed reactor, and thus, the reaction time being shorter than it should be.

3.2.3. The Influence of Alumina Addition into the Catalyst System in the Micro-Channel Reactor

Alumina was added to the $Ce_{0.75}Zr_{0.25}O_2$ catalyst system and used in this experiment, as it was believed to increase the adhesion force between the active catalyst powders and the surface of stainless steel substrates [52,53]. From Figure 8, it can be seen that the 5-cycle average H_2 amount, produced in the presence of the bare reactor, $Ce_{0.75}Zr_{0.25}O_2$, and $Ce_{0.75}Zr_{0.25}O_2/Al_2O_3$, was estimated at 130.83, 245.61 and 108.45 μmol, respectively. This concluded that the addition of alumina had a negative effect on H_2 productivity. In addition, H_2 production when using $Ce_{0.75}Zr_{0.25}O_2/Al_2O_3$ was lower than when using the blank reactor. This means that the addition of alumina inhibited the access of water to react with $Ce_{0.75}Zr_{0.25}O_2$. Meanwhile, the surface of the blank reactor was obviously a catalyst itself, as it was formed by the oxidation of metals in stainless steel, such as Cr, Mn, and Fe. These metal oxides are known as redox catalysts, and could therefore catalyze this reaction.

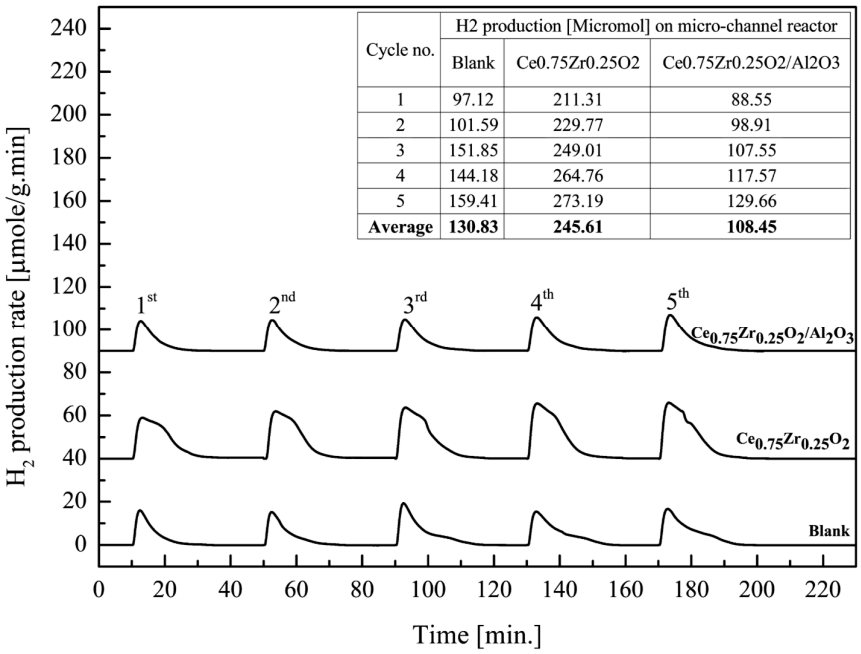

Figure 8. H_2 productivity over $Ce_{0.75}Zr_{0.25}O_2$ and $Ce_{0.75}Zr_{0.25}O_2/Al_2O_3$ coated in a micro-channel reactor, compared to a blank micro-channel reactor at the same reduction/oxidation temperature 700/700 °C.

4. Conclusions

$Ce_{0.75}Zr_{0.25}O_2$ was found to have better catalytic performance towards the two-step thermochemical cycles of water splitting, compared to CeO_2. The higher oxygen storage capacity was suggested to be the cause. Oxygen mobility in the lattice depended on the effective radius of the cations. Thus, the partial substitution of Ce^{4+} (higher ionic radius of 0.97 Å) with Zr^{4+} (smaller ionic radius of 0.84 Å) could create a smaller unit cell volume and larger channel radius in the lattice while the desired fluorite structure of ceria was remained. The infinitesimal cell volume required less energy for the hopping of oxygen ions; therefore, the active oxygen could be easily migrated from one vacancy to the others through the channel radius in the lattice. In a packed-bed reactor, it gave 1694 μmol/g of H_2 productivity at 900 °C. Because the micro-channel reactor was fabricated from stainless steel, the highest operating temperature of the micro-channel reactor was limited to 700 °C. The micro-channel reactor was proved to show 16 times higher H_2 productivity compared with the packed-bed reactor when operated at 700 °C. This was the result of the high surface-to-volume ratio of the micro-channel reactor, which allows better access of the gaseous reactant to react with the catalyst.

Author Contributions: Conceptualization, U.W.H. and T.S.; Methodology, N.N.; Validation, U.W.H., N.S.-n. and N.N.; Formal Analysis, M.H.; Investigation, N.L.; Data Curation, N.N.; Writing-Original Draft Preparation, N.N.; Writing-Review & Editing, M.H.; Visualization, U.W.H.; Supervision, N.L.; Project Administration, N.S.-n.; Funding Acquisition, T.S.

Funding: This research was funded by PTT, Thailand Research Fund [RSA6180061] and National Research Council of Thailand [KMUTNB-GOV-58-47, KMUTNB-GOV-59-43, KMUTNB-GOV-60-55, KMUTNB-61-GOV-03-44/KMUTNB-61-GOV-C1-46].

Acknowledgments: PTT, Thailand Research Fund (RSA6180061) and National Research Council of Thailand (KMUTNB-GOV-58-47, KMUTNB-GOV-59-43, KMUTNB-GOV-60-55, KMUTNB-61-GOV-03-44/KMUTNB-61-GOV-C1-46) are acknowledged for financial support.

Conflicts of Interest: The authors declare no conflict of interest.

References

1. Balat, M. Potential importance of hydrogen as a future solution to environmental and transportation problems. *Int. J. Hydrog. Energy* **2008**, *33*, 4013–4029. [CrossRef]
2. Mathur, H.B.; Das, L.M.; Patro, T.N. Hydrogen fuel utilization in CI engine powered end utility systems. *Int. J. Hydrog. Energy* **1992**, *17*, 369–374. [CrossRef]
3. Chang, A.C.C.; Chang, H.F.; Lin, F.J.; Lin, K.H.; Chen, C.H. Biomass gasification for hydrogen production. *Int. J. Hydrog. Energy* **2011**, *36*, 14252–14260. [CrossRef]
4. Appleby, A.J. Fuel cell technology and innovation. *J. Power Sources* **1992**, *37*, 223–239. [CrossRef]
5. Ismagilov, Z.R.; Matus, E.V.; Ismagilov, I.Z. Hydrogen production through hydrocarbon fuel reforming processes over Ni based catalysts. *Catal. Today* **2019**, 166–182. [CrossRef]
6. Lecart, B.; Devalette, M.; Manaud, J.P.; Meunier, G.; Hagenmuller, P. A new thermochemical process for hydrogen production. *Int. J. Hydrog. Energy* **1979**, *4*, 7–11. [CrossRef]
7. DeLuchi, M.A. Hydrogen vehicles: An evaluation of fuel storage, performance, safety, environmental impacts, and cost. *Int. J. Hydrog. Energy* **1989**, *14*, 81–130. [CrossRef]
8. Nikolaidis, P.; Poullikkas, A. A comparative overview of hydrogen production processes. *Renew. Sustain. Energy Rev.* **2017**, *67*, 597–611. [CrossRef]
9. Agrafiotis, C.; Roeb, M.; Konstandopoulos, A.G. Solar water splitting for hydrogen production with monolithic reactors. *Sol. Energy* **2005**, *79*, 409–421. [CrossRef]
10. Dersch, J.; Mathijsen, A.; Roeb, M.; Sattler, C. Modelling of a solar thermal reactor for hydrogen generation. In Proceedings of the 5th International Modelica Conference, Vienna, Austria, 4–5 September 2006; pp. 441–448. Available online: http://elib.dlr.de/46853/ (accessed on 15 June 2019).
11. Venstrom, L.J.; Petkovich, N.; Rudisill, S.; Stein, A.; Davidson, J.H. The effects of morphology on the oxidation of ceria by water and carbon dioxide. *J. Sol. Energy Eng.* **2012**, *134*, 011005. [CrossRef]
12. Roeb, M.; Sattler, C.; Klüser, R. Solar hydrogen production by a two-step cycle based on mixed iron oxides. In Proceedings of the ASME 2005 International Solar Energy Conference, Orlando, FL, USA, 6–12 August 2005; pp. 671–678. [CrossRef]
13. Steinfeld, A. Solar hydrogen production via a two-step water-splitting thermochemical cycle based on Zn/ZnO redox reactions. *Int. J. Hydrog. Energy* **2002**, *27*, 611–619. [CrossRef]
14. Sibieude, F.; Ducarroir, M.; Tofighi, A.; Ambriz, J. High temperature experiments with a solar furnace: The decomposition of Fe3O4, Mn3O4, CdO. *Int. J. Hydrog. Energy* **1982**, *7*, 79–88. [CrossRef]
15. Popa, S.G.; Ungureanu, B.S.; Gheonea, I.A. Experimental Study of SnO_2/SnO/Sn Thermochemical Systems for Solar Production of Hydrogen. *Rom. J. Morphol Embryol.* **2015**, *56*, 1495–1502. [CrossRef] [PubMed]
16. Kang, K.S.; Kim, C.H.; Cho, W.C.; Bae, K.K.; Kim, S.H.; Park, C.S. Novel two-step thermochemical cycle for hydrogen production from water using germanium oxide: KIER 4 thermochemical cycle. *Int. J. Hydrog. Energy* **2009**, *34*, 4283–4290. [CrossRef]
17. Charvin, P.; Abanades, S.; Flamant, G.; Lemort, F. Two-step water splitting thermochemical cycle based on iron oxide redox pair for solar hydrogen production. *Energy* **2007**, *32*, 1124–1133. [CrossRef]
18. Tamaura, Y.; Ueda, Y.; Matsunami, J. Solar hydrogen production by using ferrites. *Sol. Energy* **1999**, *65*, 55–57. [CrossRef]
19. Scheffe, J.R.; Li, J.; Weimer, A.W. A spinel ferrite/hercynite water-splitting redox cycle. *Int. J. Hydrog. Energy* **2010**, *35*, 3333–3340. [CrossRef]

20. Chueh, W.C.; Haile, S.M. A thermochemical study of ceria: Exploiting an old material for new modes of energy conversion and CO_2 mitigation. *Philos. Trans. R. Soc. A Math. Phys. Eng. Sci.* **2010**, *368*, 3269–3294. [CrossRef]
21. Meng, Q.L.; Lee, C.I.l.; Ishihara, T.; Kaneko, H.; Tamaura, Y. Reactivity of CeO_2-based ceramics for solar hydrogen production via a two-step water-splitting cycle with concentrated solar energy. *Int. J. Hydrog. Energy* **2011**, *36*, 13435–13441. [CrossRef]
22. Furler, P.; Scheffe, J.; Gorbar, M.; Moes, L.; Vogt, U.; Steinfeld, A. Solar thermochemical CO_2 splitting utilizing a reticulated porous ceria redox system. *Energy Fuels* **2012**, *26*, 7051–7059. [CrossRef]
23. Scheffe, J.R.; Weibel, D.; Steinfeld, A. Lanthanum-strontium-manganese perovskites as redox materials for solar thermochemical splitting of H_2O and CO_2. *Energy Fuels* **2013**, *27*, 4250–4257. [CrossRef]
24. Mamontov, E.; Egami, T.; Brezny, R.; Koranne, M.; Tyagi, S. Lattice defects and oxygen storage capacity of nanocrystalline ceria and ceria-zirconia. *J. Phys. Chem. B* **2000**, *104*, 11110–11116. [CrossRef]
25. Epifani, M.; Andreu, T.; Abdollahzadeh-Ghom, S.; Arbiol, J.; Morante, J.R. Synthesis of ceria-zirconia nanocrystals with improved microstructural homogeneity and oxygen storage capacity by hydrolytic sol-gel process in coordinating environment. *Adv. Funct. Mater.* **2012**, *22*, 2867–2875. [CrossRef]
26. Bader, R.; Venstrom, L.J.; Davidson, J.H.; Lipiński, W. Thermodynamic analysis of isothermal redox cycling of ceria for solar fuel production. *Energy Fuels* **2013**, *27*, 5533–5544. [CrossRef]
27. Fueki, K. Efficiency of thermochemical production of hydrogen. *Int. J. Hydrog. Energy* **1976**, *1*, 129–131. [CrossRef]
28. Scheffe, J.R.; Steinfeld, A. Thermodynamic analysis of cerium-based oxides for solar thermochemical fuel production. *Energy Fuels* **2012**, *26*, 1928–1936. [CrossRef]
29. Falter, C.; Pitz-Paal, R. Energy analysis of solar thermochemical fuel production pathway with a focus on waste heat recuperation and vacuum generation. *Sol. Energy* **2018**, *176*, 230–240. [CrossRef]
30. Pengpanich, S.; Meeyoo, V.; Rirksomboon, T.; Bunyakiat, K. Catalytic oxidation of methane over CeO_2-ZrO_2 mixed oxide solid solution catalysts prepared via urea hydrolysis. *Appl. Catal. A Gen.* **2002**, *234*, 221–233. [CrossRef]
31. Li, J.; Liu, X.; Zhan, W.; Guo, Y.; Guo, Y.; Lu, G. Preparation of high oxygen storage capacity and thermally stable ceria-zirconia solid solution. *Catal. Sci. Technol.* **2016**, *6*, 897–907. [CrossRef]
32. Reddy, B.M.; Reddy, G.K.; Reddy, L.H.; Ganesh, I. Synthesis of Nanosized Ceria-Zirconia Solid Solutions by a Rapid Microwave-Assisted Combustion Method. *Open Phys. Chem. J.* **2009**, *3*, 24–29. [CrossRef]
33. Sujana, M.G.; Chattopadyay, K.K.; Anand, S. Characterization and optical properties of nano-ceria synthesized by surfactant-mediated precipitation technique in mixed solvent system. *Appl. Surf. Sci.* **2008**, *254*, 7405–7409. [CrossRef]
34. Shih, C.J.; Chen, Y.J.; Hon, M.H. Synthesis and crystal kinetics of cerium oxide nanocrystallites prepared by co-precipitation process. *Mater. Chem. Phys.* **2010**, *121*, 99–102. [CrossRef]
35. Osman, A.I.; Abu-Dahrieh, J.K.; Rooney, D.W.; Halawy, S.A.; Mohamed, M.A.; Abdelkader, A. Effect of precursor on the performance of alumina for the dehydration of methanol to dimethyl ether. *Appl. Catal. B Environ.* **2012**, *127*, 307–315. [CrossRef]
36. Takashi, S.; Hideo, W.; Masayoshi, F.; Minoru, T. Structural Properties and Surface Characteristics on Aluminum Oxide Powders. *Rev. Med. Chile* **2009**, *9*, 23–31.
37. Wang, X.; Liu, D.; Li, J.; Zhen, J.; Zhang, H. Clean synthesis of Cu_2O@CeO_2 core@shell nanocubes with highly active interface. *NPG Asia Mater.* **2015**, *7*, 158–164. [CrossRef]
38. Zhang, X.M.; Deng, Y.Q.; Tian, P.; Shang, H.H.; Xu, J.; Han, Y.F. Dynamic active sites over binary oxide catalysts: In situ/operando spectroscopic study of low-temperature CO oxidation over MnOx-CeO_2 catalysts. *Appl. Catal. B Environ.* **2016**, *191*, 179–191. [CrossRef]
39. Liu, L.; Shi, J.; Zhang, X.; Liu, J. Flower-Like Mn-Doped CeOMicrostructures: Synthesis, Characterizations, and Catalytic Properties. *J. Chem.* **2015**, *2015*, 254750. [CrossRef]
40. MacIel, C.G.; Silva, T.D.F.; Hirooka, M.I.; Belgacem, M.N.; Assaf, J.M. Effect of nature of ceria support in CuO/CeO_2 catalyst for PROX-CO reaction. *Fuel* **2012**, *97*, 245–252. [CrossRef]
41. Biswas, P.; Kunzru, D. Steam reforming of ethanol for production of hydrogen over Ni/CeO_2-ZrO_2 catalyst: Effect of support and metal loading. *Int. J. Hydrog. Energy* **2007**, *32*, 969–980. [CrossRef]
42. Kim, D.J. Lattice Parameters, Ionic Conductivities, and Solubility Limits in Fluorite-Structure MO_2 Oxide [M = Hf4+, Zr4+, Ce4+, Th4+, U4+] Solid Solutions. *J. Am. Ceram. Soc.* **1989**, *72*, 1415–1421. [CrossRef]

43. Kang, K.; Kim, C.; Park, C.; Kim, J. Hydrogen Reduction and Subsequent Water Splitting. *J. Ind. Eng. Chem.* **2007**, *13*, 657–663.
44. Córdoba, L.F.; Martínez-Hernández, A. Preferential oxidation of CO in excess of hydrogen over Au/CeO_2-ZrO_2 catalysts. *Int. J. Hydrog. Energy* **2015**, *40*, 16192–16201. [CrossRef]
45. Le Gal, A.; Abanades, S.; Flamant, G. CO_2 and H_2O splitting for thermochemical production of solar fuels using nonstoichiometric ceria and ceria/zirconia solid solutions. *Energy Fuels* **2011**, *25*, 4836–4845. [CrossRef]
46. Zhao, Z.; Uddi, M.; Tsvetkov, N.; Yildiz, B.; Ghoniem, A.F. Enhanced intermediateerature CO_2 splitting using nonstoichiometric ceria and ceria-zirconia. *Phys. Chem. Chem. Phys.* **2017**, *19*, 25774–25785. [CrossRef] [PubMed]
47. Sukonket, T.; Khan, A.; Saha, B. Influence of the Catalyst Preparation Method, Surfactant Amount, and Steam on CO_2 Reforming of CH4 over 5Ni/Ce0.6Zr $0.4O_2$ Catalysts. *Energy Fuels* **2011**, *25*, 864–877. [CrossRef]
48. Kolb, G. Review: Microstructured reactors for distributed and renewable production of fuels and electrical energy. *Chem. Eng. Process. Process Intensif.* **2013**, *65*, 1–44. [CrossRef]
49. Pennemann, H.; Watts, P.; Haswell, S.J.; Hessel, V.; Löwe, H. Benchmarking of microreactor applications. *Org. Process Res. Dev.* **2004**, *8*, 422–439. [CrossRef]
50. Mathieu-Potvin, F.; Gosselin, L.; Da Silva, A.K. Optimal geometry of catalytic microreactors: Maximal reaction rate density with fixed amount of catalyst and pressure drop. *Chem. Eng. Sci.* **2012**, *73*, 249–260. [CrossRef]
51. Lau, W.N.; Yeung, K.L.; Martin-Aranda, R. Knoevenagel condensation reaction between benzaldehyde and ethyl acetoacetate in microreactor and membrane microreactor. *Microporous Mesoporous Mater.* **2008**, *115*, 156–163. [CrossRef]
52. Peela, N.R.; Mubayi, A.; Kunzru, D. Washcoating of γ-alumina on stainless steel microchannels. *Catal. Today* **2009**, *147*, 17–23. [CrossRef]
53. Wu, X.; Weng, D.; Zhao, S.; Chen, W. Influence of an aluminized intermediate layer on the adhesion of a γ-Al_2O_3 washcoat on FeCrAl. *Surf. Coat. Technol.* **2005**, *190*, 434–439. [CrossRef]

© 2019 by the authors. Licensee MDPI, Basel, Switzerland. This article is an open access article distributed under the terms and conditions of the Creative Commons Attribution (CC BY) license (http://creativecommons.org/licenses/by/4.0/).